Check for updates

EurJIC
European Journal of Inorganic Chemistry

Research Article
doi.org/10.1002/ejic.202500227

Chemistry Europe
European Chemical Societies Publishing

www.eurjic.org

Biomass-Derived Porous Crystalline Calcium-Silicates Synthesized from Chicken Eggshell Waste Using Organic Amine Templates: A Case Study for Potential Hemostatic Application

Guilherme de Paula Guarnieri, Oscar Antonio Niño Santisteban, Erick Paiva Cancella, Eduardo Ribeiro de Azevedo, Ivana Conte Cosentino, Lucildes Pita Mercuri, Marcelo Larami Santoro, Moacir Fernandes de Godoy, and José Geraldo Nery*

Uncontrollable hemorrhage is a major cause of mortality in accidents, trauma, and medical procedures, highlighting the need for effective hemostatic agents. Zeolites and similar materials are promising due to their adsorption properties and ability to concentrate coagulation factors. This study reports the synthesis of calcium-silicates from chicken eggshell waste using TEA.OH, TPA.OH, and TBA.OH as templates. TPA.OH and TBA.OH direct the formation of rhodesite, a fibrous calcium-silicate, while TEA.OH results in quartz. Materials synthesized with TPA.OH and TBA.OH have surface areas of 53.3–100.3 $m^2 g^{-1}$ and mesopores ranging from 5.7 to 27.7 nm with pore volumes of 0.018–0.11 $cm^3 g^{-1}$. In vitro coagulation assays (PT, aPTT) revealed that CaZ-3 and CaZ-4 activate factors within the contact system. The recalcification assay shows a significant reduction in clotting time, indicating action via the intrinsic pathway. Thromboelastographic analysis confirms high hemostatic performance: the material prepared with TBA.OH shows a shorter clot formation time ($R = 1.8 \pm 0.5$ min) and higher maximum clot strength ($MA = 52.1 \pm 1.3$ mm) than QuikClot, demonstrating its potential as an effective, waste-derived hemostatic agent.

1. Introduction

Hemorrhage, defined as uncontrolled and excessive bleeding, is a condition that may be caused by physical traumas, surgical complications, or underlying physiological abnormalities. It constitutes a critical medical emergency, demanding immediate attention and effective intervention.[1,2] The complexities inherent in managing hemorrhagic events arise from the intricate interplay of various physiological systems, such as the coagulation cascade, platelet function, and vascular dynamics, which collectively contribute to the delicate balance between clot formation and bleeding control in the human body.[3] Despite advances in surgical techniques and medical interventions, managing hemorrhage continues to present significant hurdles, particularly in scenarios where conventional methods are insufficient or impractical.[4,5] In these cases, hemostatic agents can be employed to promote coagulation, helping to control the bleeding. In a broader context, hemostatic agents must fulfill criteria such as prompt action, non-antigenicity, ease of application and removal, cost-effectiveness, stability, transportability, and minimal side

G. de Paula Guarnieri, O. A. N. Santisteban, E. P. Cancella, J. G. Nery
Department of Physics
São Paulo State University
Cristóvão Colombo Street, 2265 - Jardim Nazareth, São José do Rio Preto 15054-000, SP, Brazil
E-mail: geraldo.nery@unesp.br

E. R. de Azevedo
São Carlos Institute of Physics
University of São Paulo
Av. Trab. São Carlense, 400 - Parque Arnold Schimidt, São Carlos 13566-590, SP, Brazil

I. C. Cosentino
Institute for Energy and Nuclear Research
University of São Paulo
Prof. Lineu Prestes Avenue, 2242 - Cidade Universitária - Butantã, São Paulo 05508-000, SP, Brazil

L. P. Mercuri
Department of Exact and Earth Sciences, Faculty of Chemistry
Federal University of São Paulo
Prof. Artur Riedel Street, 275 - Eldorado, Diadema 09972-270, SP, Brazil

M. L. Santoro
Central Animal Facility and Higher School of the Butantan Institute
State Health Department of São Paulo
Av. Vital Brasil, 1500 - Butantã, São Paulo 05503-900, SP, Brazil

M. F. de Godoy
Department of Cardiology and Vascular Surgery
Medicine Faculty of São José do Rio Preto
Av. Brg. Faria Lima, 5416 - Vila Sao Pedro, São José do Rio Preto 15090-000, SP, Brazil

Supporting information for this article is available on the WWW under https://doi.org/10.1002/ejic.202500227

© 2025 The Author(s). European Journal of Inorganic Chemistry published by Wiley-VCH GmbH. This is an open access article under the terms of the Creative Commons Attribution License, which permits use, distribution and reproduction in any medium, provided the original work is properly cited.

© 2025 The Author(s). European Journal of Inorganic Chemistry published by Wiley-VCH GmbH

effects. Over the past decades, comprehensive reviews detailing the action mechanisms, functionality, mode of delivery, and clinical studies of available topical hemostatic agents have been published in the literature.[6,7] Topical hemostatic agents can be categorized into three classes: mucoadhesive agents, procoagulant supplementers, and factor concentrators. Due to their adsorption properties and ability to concentrate coagulation factors and platelets in hemorrhaging blood, zeolites stand out as excellent hemostatic agents.

Over the past two decades, various inorganic biomaterials, including zeolites, have been developed. Zeolites are crystalline aluminosilicates with a porous structure that promotes water adsorption, thereby concentrating platelets and clotting factors at the application site.[8] Additionally, their negatively charged surface can activate positively charged factor XII, initiating the endogenous coagulation cascade.[9] Recent studies have elucidated additional molecular mechanisms, such as the capability of calcium-exchanged zeolites to serve as a solid-phase scaffold for the formation of prothrombinase-like complexes by interacting with coagulation factor Xa, leading to the production of significantly elevated levels of thrombin in comparison to platelet-based activation.[10,11] Although the mechanisms of zeolite-induced hemostasis are not fully comprehended yet, these unique characteristics led to the development of the first commercial zeolite-based hemostatic product, introduced in 2002 as first-aid equipment for the US military under the tradename QuikClot. More recently, other inorganic materials, such as mesoporous silica, graphene oxides (GO), graphene/montmorillonite composite sponges (GMCS), and graphene-immobilized montmorillonite (MMT), have been synthesized and systematically investigated for their hemostatic properties.[12,13] Nevertheless, it is important to note that these hemostatic agents based on inorganic biomaterials have advantages and disadvantages, as widely discussed in the literature.[8,14–16] It has been pointed out that there are challenges in the preparation of active inorganic-based biomaterials with enhanced hemostatic properties, taking into consideration both functional and application aspects.[14] Inorganic biomaterial-based hemostatic agents present both advantages and limitations, with challenges persisting in the design of functionally optimized materials for clinical use. Although not addressed in this study, emerging tools such as artificial intelligence (AI) and machine learning (ML) may, in future research, support the rational design of inorganic nanostructures with improved biocompatibility and hemostatic efficacy.[17–19]

Historically, a challenge in employing zeolites as hemostatic agents has been the exothermic reaction that can raise the temperature in the vicinity of the application site by as much as 90 °C, potentially causing severe tissue damage (such as burns). Techniques that have been employed to overcome this problem include prehydrating the zeolite to decrease the exothermicity of water absorption,[8,20] the incorporation of other minerals such as bentonite[21] or phyllosilicates (smectite,[22] kaolin,[8] halloysite[23]), or reducing the zeolite particle size to the nanometric scale, thereby minimizing heat generation.[24] The human blood coagulation system is a complex network of interconnected glycoproteins that, upon activation, initiate a cascade of enzymatic reactions culminating in the formation of fibrin. This process, known as hemostasis, is essential for the cessation of bleeding. Hemostasis exemplifies a molecular machinery paradigm, where the orchestrated assembly of substrates, enzymes, protein cofactors, and calcium ions on a phospholipid interface drastically accelerates coagulation rates.[25]

Calcium ions play a pivotal role in triggering the coagulation cascade, as illustrated in **Figure 1**.[8] At a molecular level, hemostasis entails a sequence of events primarily governed by serine proteases within the coagulation cascade, ultimately resulting in the conversion of fibrinogen to fibrin by thrombin. Upon vessel injury, extravasated blood encounters abundant tissue factor (TF) within the surrounding tissues. TF, acting as a cofactor, forms a complex with factor VIIa, initiating the extrinsic pathway of coagulation.

Although there are around 258 zeolites with different frameworks that confer unusual and interesting topologies and structures of channels and cavities,[26] only five of them are produced in large amounts for a wide range of applications. This group of zeolites is known as the "Big Five" (FER, MOR, MFI, FAU, and BEA),[27] with only FAU zeolites having been used as hemostatic agents,[28,29] despite the small quantity of extra-framework calcium cations, when compared to the natural counterpart. However, calcium-rich zeolites such as wairakite, scolecite, and gismondine occur worldwide as major constituents of submarine volcanic sediments and as alteration products of volcanic glass in low-grade metavolcanics and metaclastics.[30] These natural calcium zeolites have been known since the early years of the twentieth century, with several reports having described their crystallographic structures, thermodynamic behaviors under different synthesis conditions, and industrial applications.[31]

It is also interesting to notice that in the Database of Zeolite Structures,[26] none of the listed calcium zeolites have been synthesized utilizing biomass waste as the calcium source.[26,30–33] Therefore, the present investigation addresses two crucial questions: Is it possible to synthesize zeolite-analog calcium-silicate materials using an abundant inorganic biomass (in this case, chicken eggshell waste) as a source of calcium cations? If so, how would these materials perform in hemostatic applications compared to the ones already available in the market and currently used in hospitals and emergency centers?

Numerous reports in scientific literature have explored the diverse applications of eggshell waste across several fields.[34,35] In environmental applications, eggshell waste is used for organic compound adsorption, as well as the adsorption of nitrogen, fluoride, phosphate, soil pollutants, and radioactive metals. It also aids in sludge solubilization, biomass production, and the fabrication of magnetic eggshell adsorbents. In engineering, eggshells are incorporated into plastics, material applications, and nanoparticle synthesis. In chemical processes, they are employed in the development of plant growth promoters for fertilizers, enhancement of food processing and production, sourcing of active calcium and carbon, extraction of soluble proteins, and sourcing of organic calcium and ultrafine active calcium carbonate, with additional roles in biodiesel oil catalysis. In the biomedical domain, eggshell waste has emerged as a versatile precursor for the synthesis of calcium-based compounds such as calcium lactate and calcium

© 2025 The Author(s). European Journal of Inorganic Chemistry published by Wiley-VCH GmbH

10990682c, 2025, 26, Downloaded from https://chemistry-europe.onlinelibrary.wiley.com/doi/10.1002/ejic.202500227 by University Of Sao Paulo - Brazil, Wiley Online Library on [29/09/2025]. See the Terms and Conditions (https://onlinelibrary.wiley.com/terms-and-conditions) on Wiley Online Library for rules of use; OA articles are governed by the applicable Creative Commons License

Research Article
doi.org/10.1002/ejic.202500227

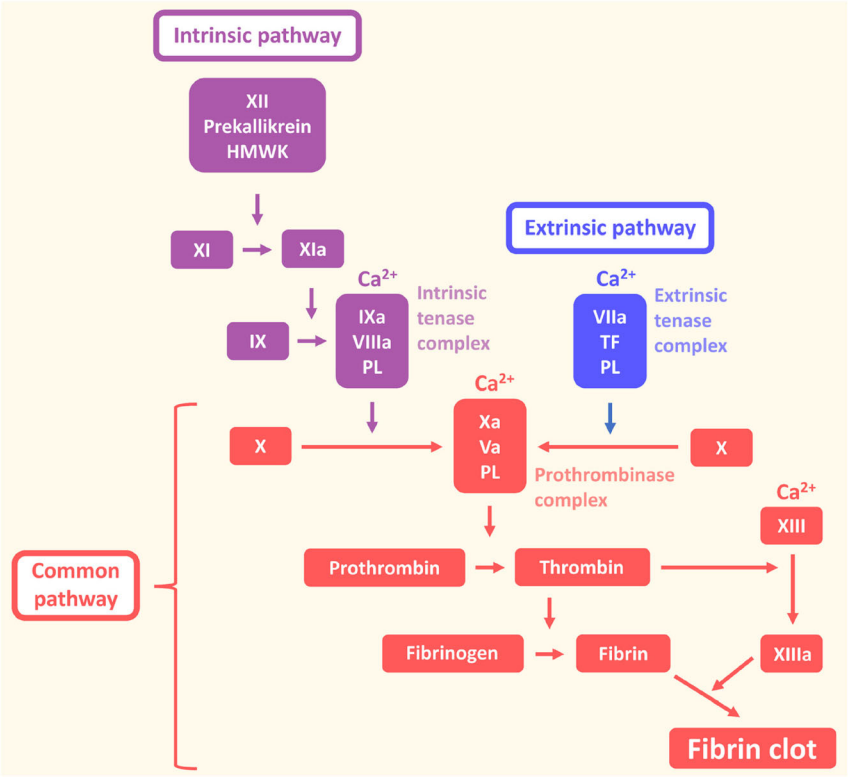

Figure 1. General scheme of the coagulation cascade. Adapted with permission.[74,75] Copyright 2015, Taylor & Francis; Copyright 2001, Thieme.

phosphate. Moreover, it has been effectively employed in the fabrication of regenerative scaffolds, targeted drug delivery systems, and electrochemical biosensors.[36–40]

Nonetheless, to the best of our knowledge, the synthesis of porous crystalline calcium-silicate materials prepared with chicken eggshell waste, for application as a topical hemostatic agent, is a previously unexplored field of research, which is addressed by the findings of this study.

2. Results and Discussion

The X-ray diffractograms for CaZ-3 and CaZ-4 (**Figure 2**) showed Bragg reflections in the 2θ range 7.5–35.6°, which closely matched those of rhodesite (JCPDS 22-1253). Rhodesite, a known natural fibrous calcium-silicate, has the chemical formula (Ca,Na2, K2)8Si16O40.11H2O and an orthorhombic unit cell ($a = 23.8$ Å, $b = 6.54$ Å, $c = 7.05$ Å, $\beta = 90°$). The experimental results were consistent with the data reported by Gard et al.[41] and Hesse et al.[42] There are only a few reports in the literature of the synthesis of a rhodesite-like calcium-silicate, such as in the work of Rocha et al.,[43] who described the synthesis of "AV-2" using calcium nitrate as a calcium source. The diffractograms for CaZ-3 and CaZ-4 matched those reported by Rocha et al., where rhodesite was considered to consist of silicate double layers, chains of edge-sharing [Ca(O,OH2)6] octahedra, and potassium cations and water molecules within the pores of the silicate double layers.[44,45] However, to the best of our knowledge, until now, there have been no reports in the literature of synthesis routes to obtain rhodesite using CaCO3 derived from chicken eggshells. It is well known that TEA.OH, TPA.OH, and TBA.OH can direct the crystallization of several zeolites with different topologies, such as ETR, MFI, BEA, SZR, and MEL.[46] At the present stage of the research, it is not possible to know precisely how TPA.OH and TBA.OH affected the crystallization process and favored the formation of rhodesite. Unlike TPA.OH and TBA.OH, the TEA.OH organic template (used for CaZ-2) did not effectively contribute to rhodesite synthesis, with the material obtained using this organic molecule being ascribed to a quartz phase (JCPDS 46-1045) and a calcite phase (JCPDS 05-0586). Synthesis in the absence of any organic template led to the formation of a material (CaZ-1) corresponding to calcite (JCPDS 05-0586). Some reflections in the diffractograms for CaZ-1 and CaZ-2, mainly those at 2θ lower than 25°, could not be assigned to any known phases, according to searches in the JCPDS database.

Some reflections in the diffractograms for CaZ-1 and CaZ-2, mainly those at 2θ lower than 25°, could not be assigned to any known phases, according to searches in the JCPDS database. See Supporting Information (SF1) for all materials' XRD data.

The SEM and TEM analyses of the materials provide comprehensive insights into their morphological and structural characteristics. The SEM micrographs (**Figure 3**A) illustrate that CaZ-4 comprises well-defined microcrystals with a pronounced needle-like (acicular) morphology, exhibiting lengths varying from ≈3 μm to 20 μm. This morphology closely mirrors that of rhodesite

© 2025 The Author(s). European Journal of Inorganic Chemistry published by Wiley-VCH GmbH

10990682c, 2025, 26, Downloaded from https://chemistry-europe.onlinelibrary.wiley.com/doi/10.1002/ejic.202500227 by University Of Sao Paulo - Brazil, Wiley Online Library on [29/09/2025]. See the Terms and Conditions (https://onlinelibrary.wiley.com/terms-and-conditions) on Wiley Online Library for rules of use; OA articles are governed by the applicable Creative Commons License

Research Article
doi.org/10.1002/ejic.202500227

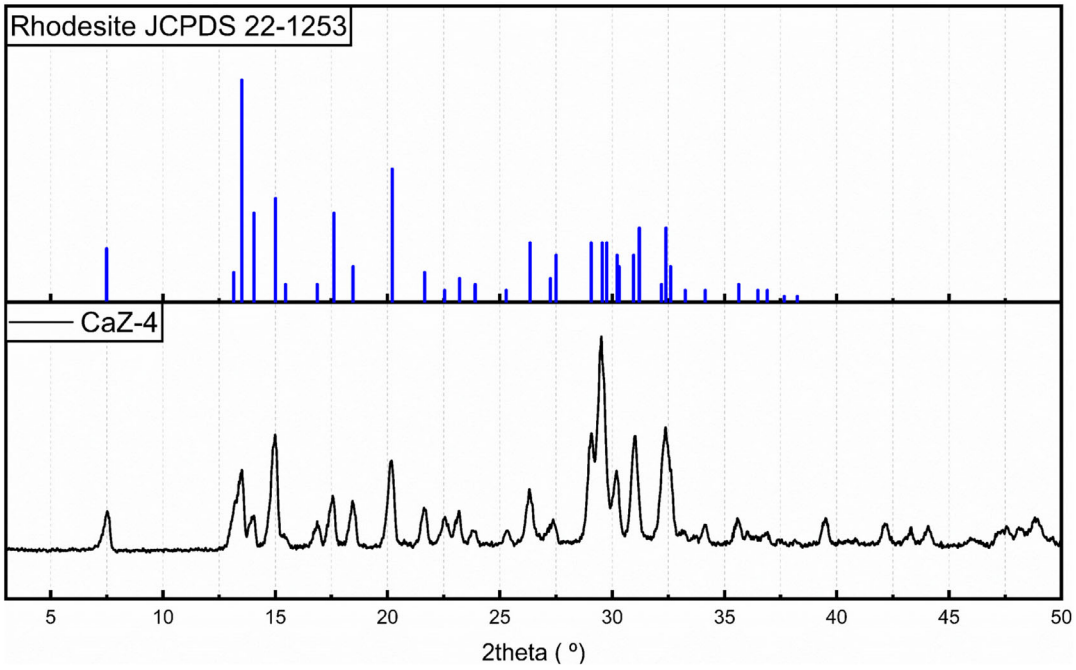

Figure 2. XRD patterns of CaZ-4, compared with the simulated diffractogram of natural calcium-silicate rhodesite, based on the JCPDS database. The Y-axis represents intensity in arbitrary units.

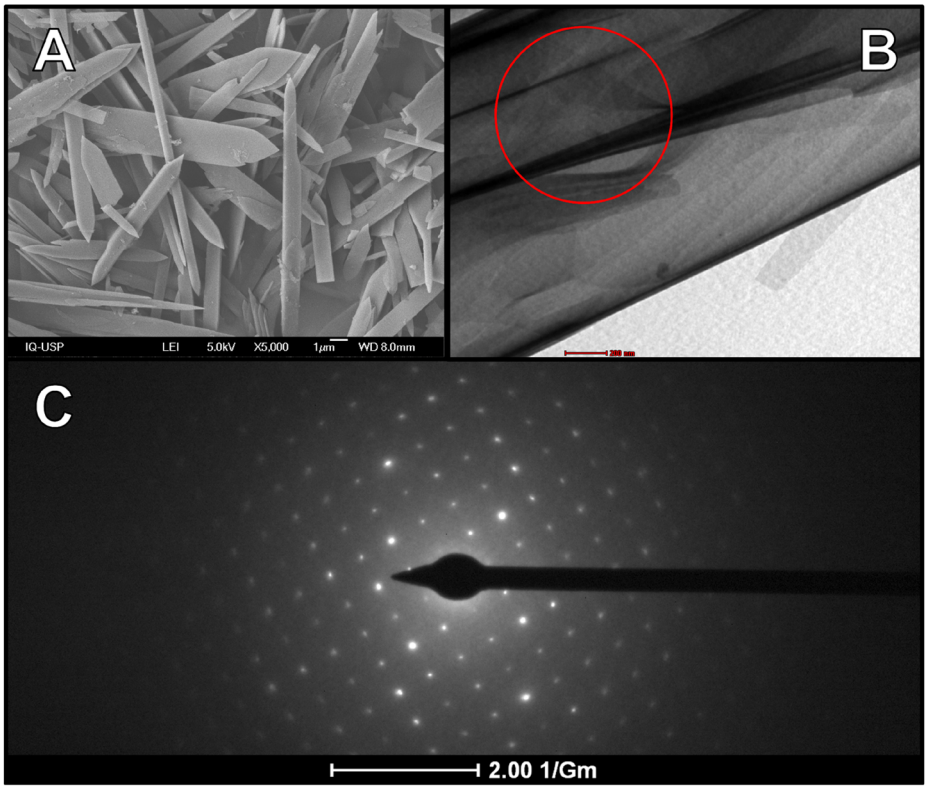

Figure 3. Electron micrographs of CaZ-4. A) SEM image; B) TEM image; and C) SAED pattern corresponding to the region marked with a red circle in (B).

crystals, as previously documented by Gard et al.[41] and Hesse et al.[42] Micrographs of CaZ-3 display similar crystal morphologies. Conversely, the materials CaZ-1 and CaZ-2 predominantly consist of plate-like microcrystals interspersed with substantial quantities of debris, indicative of a comparatively lower degree of crystallinity. See Supporting Information (SF2) for all SEM images.

© 2025 The Author(s). European Journal of Inorganic Chemistry published by Wiley-VCH GmbH

10990682c, 2025, 26, Downloaded from https://chemistry-europe.onlinelibrary.wiley.com/doi/10.1002/ejic.202500227 by University Of Sao Paulo - Brazil, Wiley Online Library on [29/09/2025]. See the Terms and Conditions (https://onlinelibrary.wiley.com/terms-and-conditions) on Wiley Online Library for rules of use; OA articles are governed by the applicable Creative Commons License

Research Article
doi.org/10.1002/ejic.202500227

The TEM investigation of CaZ-4 (Figure 3B,C) substantiates its structural resemblance to rhodesite, confirming the presence of a framework comprising double layers of vertex-sharing SiO_4 tetrahedra. This observation aligns with the well-established crystal structure of rhodesite, a microporous tectosilicate characterized by alternating layers of double silicon tetrahedra (SiO_4) and intercalated cationic sheets. These sheets predominantly consist of calcium (Ca^{2+}) and potassium (K^+), with water molecules occupying the intracrystalline cavities, as reported by Hesse et al.,[42] Rocha and Anderson,[45] Ferraris et al.,[47,48] and Geng et al.[49] In conclusion, the SEM and TEM analyses unequivocally confirm that the morphological and structural attributes of CaZ-4 closely align with those of rhodesite, reaffirming the consistency of its crystalline framework with the microporous tectosilicate structure described in the literature. The observed disparities in morphology and crystallinity between CaZ-4 and the other materials (CaZ-1, CaZ-2, and CaZ-3) underscore the critical influence of synthesis conditions on their structural evolution.

The ^1H-^{29}Si CPMAS and the deconvoluted single-pulse excitation under magic angle spinning (^{29}Si SPEMAS) spectra of CaZ-4 are presented in **Figure 4**A,B. The deconvolution reveals three distinct resonance signals centered at $\delta = -108.0$ ppm, $\delta = -96.2$ ppm, and $\delta = -95.1$ ppm, each with a linewidth of 0.9 ppm. These signals correspond to three non-equivalent Si sites in CaZ-4, exhibiting relative populations in a 1:2:1 ratio. This distribution aligns closely with findings reported by Rocha et al.[43] Specifically, the resonance at -96.3 ppm is attributed to Si(1) sites, which constitute two-thirds of the total population, while the signal at -95.1 ppm corresponds to Si(3) sites, representing the remaining one-third. Rocha et al.[43] describe these Si(1) and Si(3) sites as belonging to [SiO_4] tetrahedra that share three of their vertices with adjacent [SiO_4] tetrahedra and one vertex with a [$Ca(O, OH_2)_6$] octahedron. The third signal, centered at -108.0 ppm, is assigned to Si(2) sites, which represent [SiO_4] tetrahedra sharing all four vertices with adjacent [SiO_4] tetrahedra. These results reinforce the structural understanding of CaZ-4 and provide further evidence for the arrangement of its silicon sites, consistent with the crystalline framework previously described in the literature.[42,45,47,48]

Figure 5 shows the FTIR spectra for CaZ-4. Absorption bands in the wavenumber range 400–1200 cm^{-1} were associated with the vibrational modes of TO_4, the basic tetrahedral units that form zeolite frameworks, where *T* represents a silicon or aluminum atom.[50,51] A strong absorption band at 694 cm^{-1} corresponded to a bending mode of O–Si–O, while a broad band at around 1000–1200 cm^{-1} could be assigned to symmetric stretching of Si–O–Si. A band at 433 cm^{-1} was attributed to an O–Ca–O non-bridging bending mode.[52–54] Bands at around 877, 1430, and 2530 cm^{-1}, which were more prominent for CaZ-1, were associated with the vibrational modes of calcium carbonate,[55] probably corresponding to a fraction of calcium carbonate that was not consumed during the syntheses. This corroborated the Bragg reflections associated with calcite in the X-ray diffractograms (Figure 2), which also indicated a remaining calcite phase. Bands at around 3600 and 1634 cm^{-1} were related to the water molecules present in the samples, either as structural H_2O or as moisture deposited onto the sample surfaces, with the band at 1634 cm^{-1} attributed to H–O–H bending[56] and the one at 3600 cm^{-1} assigned to O-H stretching vibrations.[57] See the Supporting Information (SF3 and SF4) for the full range (4000–400 cm^{-1}) and inset FTIR spectra of all synthesized materials.

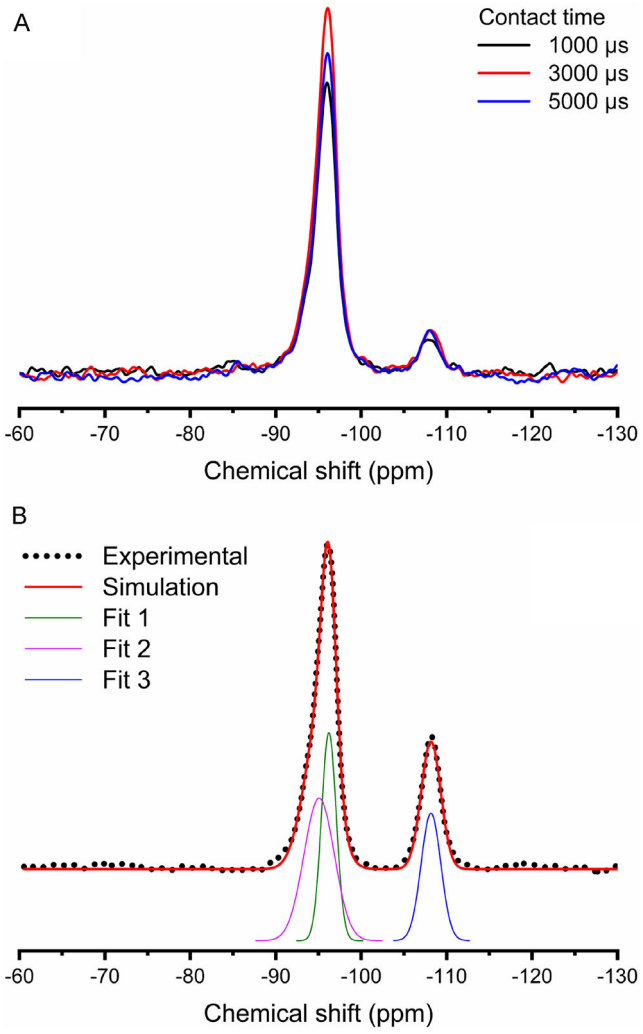

Figure 4. Solid-state NMR spectra of CaZ-4: A) cross-polarization magic angle spinning (^1H-^{29}Si CPMAS) spectrum and B) single-pulse excitation magic angle spinning (^{29}Si SPEMAS) spectrum with peak deconvolution.

Elemental analysis by ICP-OES, focusing on the mass contributions of silicon, calcium, and sodium, revealed silicon (Si) as the predominant component in the chemical composition of CaZ-4, comprising 32.0 ± 0.04% of its total mass—a characteristic feature of silicate materials. Calcium (Ca) accounted for 10.1 ± 0.1%, while sodium (Na) contributed 3.3 ± 0.1%, yielding a molar ratio of 1.0Ca: 4.6Si: 0.6Na. This stoichiometry aligns with that typically observed in calcium-silicates such as rhodesite. Similar results were reported for the rhodesite-analogous material "AV-2" by Rocha et al.,[45,58] who determined (through ICP-AES) a "calcium:sodium" molar ratio of 1.0Ca:0.6Na, closely matching the proportions found in CaZ-4. Furthermore, Rocha et al.[43] described "AV-2" as having an ideal chemical formula of

© 2025 The Author(s). European Journal of Inorganic Chemistry published by Wiley-VCH GmbH

10990682c, 2025, 26, Downloaded from https://chemistry-europe.onlinelibrary.wiley.com/doi/10.1002/ejic.202500227 by University Of Sao Paulo - Brazil, Wiley Online Library on [29/09/2025]. See the Terms and Conditions (https://onlinelibrary.wiley.com/terms-and-conditions) on Wiley Online Library for rules of use; OA articles are governed by the applicable Creative Commons License

Research Article
doi.org/10.1002/ejic.202500227

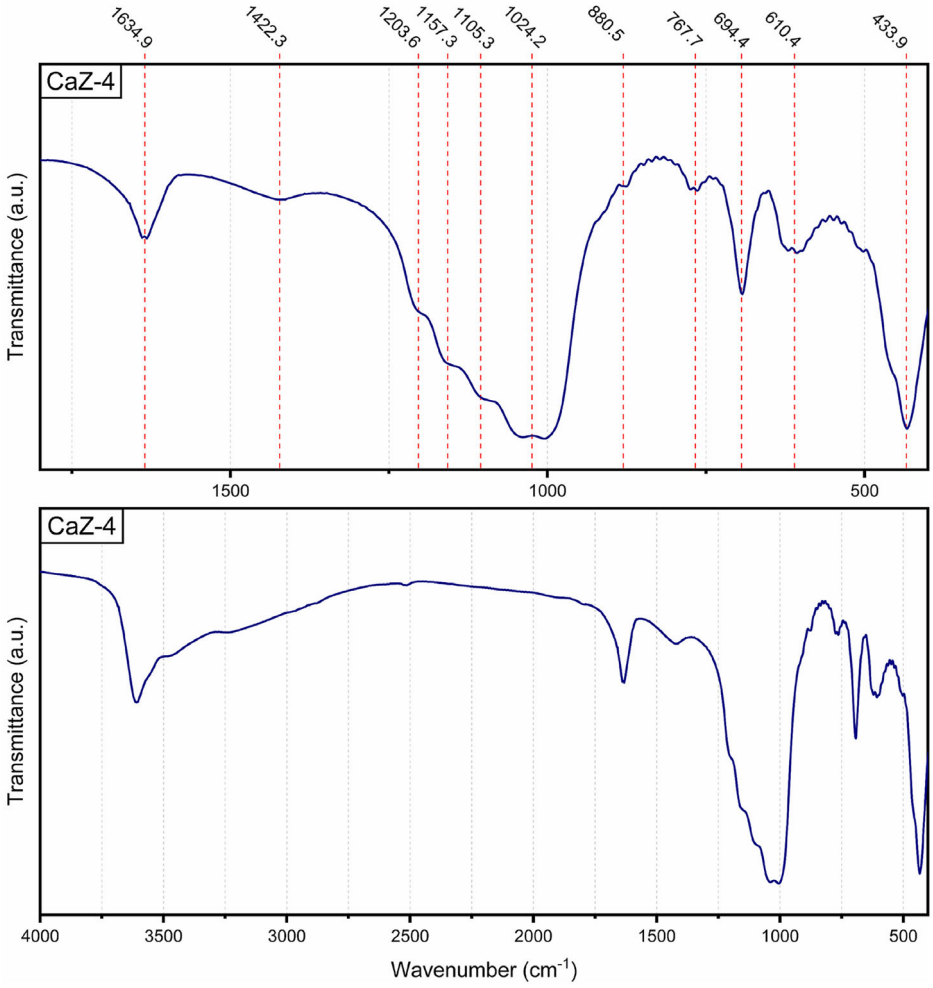

Figure 5. FTIR spectrum of CaZ-4, with magnified view of the 1800–400 cm^{-1} region highlighting key vibrational bands.

$HKCa_2$-Si_8O_{19}·$6H_2O$, which yields a molar ratio of 1.0Ca:4.0Si, further corroborating the present findings.

Considering the textural properties of the synthesized materials, the nitrogen adsorption–desorption isotherms obtained after calcination at 800 °C were classified as type IV according to the IUPAC classification, characteristic of mesoporous materials, although some microporosity was also observed. The H1-type hysteresis loops suggest capillary condensation in uniform mesopores. **Figure 6** shows the N_2 adsorption isotherms and corresponding pore size distributions for CaZ-4. Surface areas for CaZ-2 (53.3 $m^2\,g^{-1}$), CaZ-3 (72.2 $m^2\,g^{-1}$), and CaZ-4 (100.3 $m^2\,g^{-1}$) are consistent with those reported for related synthetic zeolitic and layered materials. In contrast, CaZ-1, synthesized without the use of an organic template, exhibited a substantially lower surface area of 2.9 $m^2\,g^{-1}$. Across all synthesized samples, the predominant pore volume was associated with pores centered around $D_{max} \approx 20$ Å, and the total pore volume remained relatively constant, averaging 0.10 $cm^3\,g^{-1}$ (see Supporting Information, Figure SF5–SF7 and Table ST1).

Despite confirmation of the rhodesite framework through XRD, TEM, and ^{29}Si NMR analyses, the observed mesoporosity is not intrinsic to the ideal crystalline structure but rather arises from the synthetic methodology. Unlike natural rhodesite, which crystallizes slowly under hydrothermal equilibrium to form dense, compact crystals, the materials synthesized here likely experienced rapid nucleation and kinetic growth. These conditions might have favored the formation of nanocrystalline aggregates and incomplete densification, resulting in interparticle mesoporosity while maintaining the local rhodesite lattice at the atomic scale. This hierarchical organization—crystalline at the unit cell level but porous at the mesoscale—is well documented in synthetic mineral chemistry under non-equilibrium synthesis conditions.[59,60]

Comparatively, the surface areas reported here exceed those observed for the AV-2 material synthesized without organic templates by Rocha et al. (14 $m^2\,g^{-1}$).[43,58] Although the precise mechanistic role of TPAOH and TBAOH in influencing rhodesite crystallization remains to be fully elucidated, their presence likely facilitates the formation of a more open aggregate structure with enhanced surface area, a feature potentially beneficial for applications requiring rapid fluid absorption or hemostatic functionality. While the surface areas of these calcium–silicate materials are

© 2025 The Author(s). European Journal of Inorganic Chemistry published by Wiley-VCH GmbH

10990682c, 2025, 26, Downloaded from https://chemistry-europe.onlinelibrary.wiley.com/doi/10.1002/ejic.202500227 by University Of Sao Paulo - Brazil, Wiley Online Library on [29/09/2025]. See the Terms and Conditions (https://onlinelibrary.wiley.com/terms-and-conditions) on Wiley Online Library for rules of use; OA articles are governed by the applicable Creative Commons License

Research Article
doi.org/10.1002/ejic.202500227

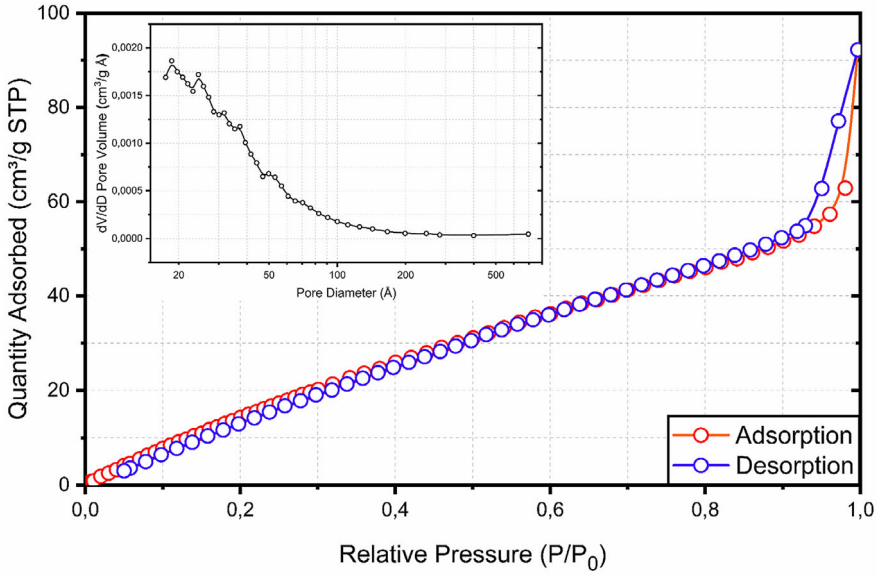

Figure 6. Nitrogen adsorption–desorption isotherm of CaZ-4.

lower than those typically reported for ion-exchanged zeolite A (280–650 $m^2 g^{-1}$),[15] they align well with the textural properties of layered clay-based hemostatic agents such as kaolin, montmorillonite, pillared montmorillonite, saponite, and hydrotalcite, all of which have demonstrated effective biomedical performance.

While the precise influence of TPA.OH and TBA.OH on the crystallization process and the formation of rhodesite remains uncertain, their presence likely fosters the development of rhodesite with enhanced surface area, potentially augmenting the hemostatic properties of the material. Despite the lower surface areas of the calcium-silicates compared to those reported for ion-exchanged zeolite A (LTA) by Stucky et al.,[24] falling within the range of 280–650 $m^2 g^{-1}$, they align with the surface areas of various layered clay-based hemostatic agents such as kaolin, montmorillonic, pillared montmorillonite, saponite, and hydrotalcite, as well as thromboelastographic parameters reported in the literature.[15]

The TG and DTG curves for the synthesized calcium-silicates revealed differences in the thermal decomposition profiles. **Figure 7** shows the thermal decomposition curve of CaZ-4. See Supporting Information (SF8–SF10) for all TG and DTG curves.

The DTG curves showed two initial events between 23 and 95 °C, corresponding to the release of free water present in all four samples. The TG curve for CaZ-3, synthesized in the presence of TPA.OH, was indicative of slower thermal decomposition and, consequently, greater thermal stability, compared to the other materials. The TG curves showed that CaZ-2, prepared with TEA.OH, presented the lowest thermal stability, while similar thermal stabilities were observed for CaZ-1 (no SDA) and CaZ-4 (prepared with TBA.OH). In the 25–600 °C temperature range, where most of the thermodynamic events occurred for all the materials, CaZ-1 displayed a mass loss of ≈16%, while CaZ-2, CaZ-3, and CaZ-4 presented mass losses ranging from 13.2% to 13.9% (Table S1, Supporting Information). These values corresponded to the stages of dehydration and thermal decomposition of

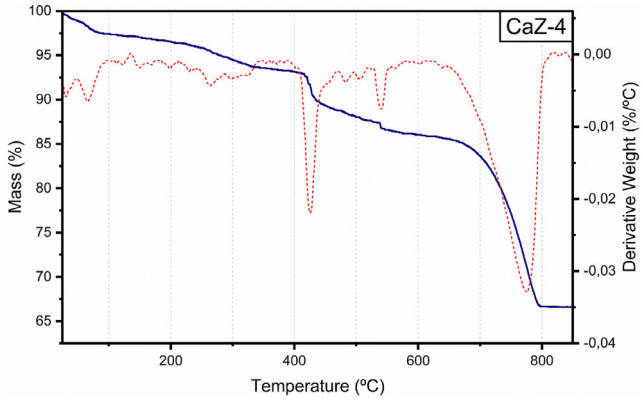

Figure 7. Thermogravimetric (TG, blue line) and derivative thermogravimetric (DTG, red dotted line) curves of CaZ-4.

the structure-directing agent, as well as some organic impurities from the chicken eggshells used as the $CaCO_3$ source. For all samples, the TG/DTG curves showed a distinct mass loss between 600 and 850 °C, due to the thermal decomposition of $CaCO_3$, resulting in the release of CO_2. Based on the $\%CO_2$ released, stoichiometric calculations ($CaCO_3 \rightarrow CaO + CO_2$) were performed to determine the amount of $CaCO_3$ present in each material (Table ST2, Supporting Information).

The other parameters determined were the temperature at the extrapolated beginning of the thermal decomposition of $CaCO_3$, obtained from the TGA curve (Tonset-TGA), and the peak temperature in the DTG curve, indicating the point at which the mass loss rate was at a maximum (Tpeak-DTG). The calculated amount of $CaCO_3$ increased proportionally with the molar masses of the structure-directing agents used in the synthesis of the materials. Table S1, which can be found in the Supporting Information, provides the full data extracted from the TG/DTG curves of the samples.

© 2025 The Author(s). European Journal of Inorganic Chemistry published by Wiley-VCH GmbH

10990682c, 2025, 26, Downloaded from https://chemistry-europe.onlinelibrary.wiley.com/doi/10.1002/ejic.202500227 by University Of Sao Paulo - Brazil, Wiley Online Library on [29/09/2025]. See the Terms and Conditions (https://onlinelibrary.wiley.com/terms-and-conditions) on Wiley Online Library for rules of use; OA articles are governed by the applicable Creative Commons License

Research Article
doi.org/10.1002/ejic.202500227

In the first heating, the DSC curve of CaZ-1 showed two endothermic events between 80 and 150 °C, related to dehydration. However, CaZ-2, CaZ-3, and CaZ-4 only showed endothermic events above 250 °C. For all the materials, the second heating curve showed an endothermic peak below 120 °C, which could be attributed to the disruption of N_2 derived from the gaseous atmosphere adsorbed when the sample was cooled, since the DSC curve showed an exothermic event. The DSC curves were obtained up to 400 °C, which meant that it was not possible to observe the enthalpic event related to the thermal decomposition of $CaCO_3$. The DSC curves for all the materials can be found in the Supporting Information (SF11–SF14).

Among other physical properties, the surface electrical potential of a solid hemostatic agent is fundamental for its application as a procoagulant or anticoagulant material. It is known that solids with a net negative surface charge promote coagulation by a process known as the "glass effect," whereby polar surfaces activate the intrinsic pathway of the blood clotting cascade by contact activation.[61] The autocatalytic activation of clotting factors XII, XI, prekallikrein, and high molecular weight kininogen is initiated by exposure of blood to a polar surface, which in turn activates the feedback mechanisms responsible for the association of thrombin and the polymerization of fibrin.[61,62] Surface area is also a crucial parameter in the chemical dynamics for immobilizing participants of surface-dependent clotting reactions and Ca^{2+} ions, which are cofactors that help to orientate protein assemblies and enzymes responsible for fibrin production.[63]

Several zeolites are used for hemostatic applications, due to their ability to maintain a net negative surface charge when immersed in blood.[9] Many factors can influence the net surface charge of a solid particle, including the pH of the medium. At high pH (high OH^- concentration), many of the silanol groups present on the surfaces of these solid silicate particles may be deprotonated, with the resulting SiO^- groups conferring a net negative surface charge. In low pH media (high H^+ concentration), these groups are more likely to be protonated, resulting in a net positive surface charge.[64] At the isoelectric point, defined as the pH at which there is a balance between the positive and negative charges, the material has a neutral surface with null electrical potential. Although zeta potential is not a direct measurement of the surface electrical potential, it provides valuable insights into particle surface charge and its behavior under different pH conditions.

As shown in **Figure 8**, all the synthesized materials presented a net negative charge across a very broad pH range. In fact, the isoelectric points (0.0 mV zeta potential) for CaZ-3 and CaZ-4 were at pH 1.0, while those for CaZ-1 and CaZ-2 were slightly below the pH range tested, although data extrapolation indicated that they would present a neutral surface at pH 0.0–1.0. In the pH range 1.5–12.0, all the materials presented net negative surface charges, with all of them showing the most negative zeta potential values at pH 3.0 (-21.9 ± 1.8, -19.5 ± 2.3, -34.5 ± 1.8, and -35.3 ± 1.3 mV for CaZ-1, CaZ-2, CaZ-3, and CaZ-4, respectively). At pH 7.0 (approximately the pH of blood), the zeta potential values were -17.2 ± 1.4 mV (CaZ-1), -18.5 ± 0.9 mV (CaZ-2), -16.2 ± 0.6 mV (CaZ-3), and -15.6 ± 0.5 mV (CaZ-4). The zeta potentials were similar for CaZ-1 and CaZ-2, as well as for CaZ-3 and CaZ-4. This was consistent with the XRD and FTIR results showing clear similarity between CaZ-1 and CaZ-2, as well as between CaZ-3 and CaZ-4. Detailed zeta potential data are provided in Supporting Information (ST3).

The in vitro hemostatic properties of CaZ-3 and CaZ-4, synthetic analogs of rhodesite, were initially assessed using blood plasma to elucidate their coagulation activation pathway. The first stage of evaluation focused on determining whether these materials exert a direct coagulant effect on citrated human plasma. For this assay, 50 μL of the plasma sample was incubated with 100 μL of material suspension or vehicle (control) at 37 °C, and the clotting time was recorded. None of the materials (QuikClot, CaZ-3 or CaZ-4) induced clot formation in plasma sample under these conditions within the 200 s limit when compared to control, indicating no direct coagulant activity under low calcium concentrations. Thereafter, the recalcification time test was used to evaluate the procoagulant activity of materials under

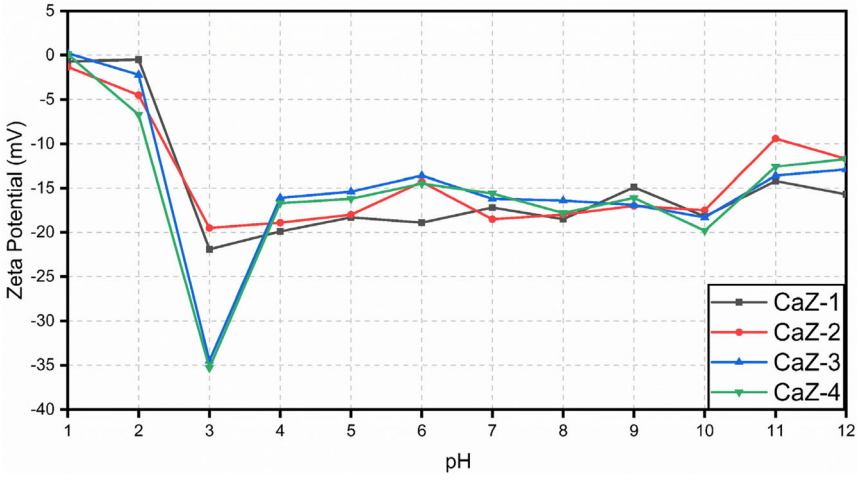

Figure 8. Zeta potential (mV) of CaZ-1, CaZ-2, CaZ-3, and CaZ-4 as a function of pH.

© 2025 The Author(s). European Journal of Inorganic Chemistry published by Wiley-VCH GmbH

10990682c, 2025, 26, Downloaded from https://chemistry-europe.onlinelibrary.wiley.com/doi/10.1002/ejic.202500227 by University Of Sao Paulo - Brazil, Wiley Online Library on [29/09/2025]. See the Terms and Conditions (https://onlinelibrary.wiley.com/terms-and-conditions) on Wiley Online Library for rules of use; OA articles are governed by the applicable Creative Commons License

Research Article
doi.org/10.1002/ejic.202500227

10990682c, 2025, 26, Downloaded from https://chemistry-europe.onlinelibrary.wiley.com/doi/10.1002/ejic.202500227 by University Of Sao Paulo - Brazil, Wiley Online Library on [29/09/2025]. See the Terms and Conditions (https://onlinelibrary.wiley.com/terms-and-conditions) on Wiley Online Library for rules of use; OA articles are governed by the applicable Creative Commons License

Table 1. Coagulation data obtained for recalcification time, prothrombin time (PT), and activated partial thromboplastin time (aPTT). The control corresponds to blood plasma incubated with Tyrode buffer.

Material	Recalcification time [s]	PT [s]	aPTT [s]
Control	167.5 ± 10.4	16.5 ± 0.6	41.2 ± 1.9
QuikClot	57.8 ± 0.9	14.8 ± 0.0	33.8 ± 0.3
CaZ-3	89.5 ± 0.8	14.1 ± 0.1	36.4 ± 0.5
CaZ-4	82.4 ± 1.1	14.8 ± 0.3	34.4 ± 0.5

Results are representative of duplicate experiments.

higher $CaCl_2$ concentration conditions (8 mM $CaCl_2$, final concentration). **Table 1** shows that all three materials exhibited coagulant activity, as evidenced by the reduction in the clotting time in comparison with the vehicle. Among the materials, QuikClot exhibited the highest procoagulant activity (≈65% reduction in the clotting time), followed by CaZ-4 (≈51% reduction) and CaZ-3 (≈47% reduction). However, if prior to adding 8 mM $CaCl_2$, plasma was preactivated with the aPTT reagent (ellagic acid and phospholipids), the reduction in clotting time was less pronounced (11%−17% reduction) for all materials. Similar results were observed when the materials were preincubated with plasma, followed by the addition of the PT reagent (thromboplastin and calcium) was added.

Since the most significant reduction in clotting time was observed in the recalcification time assay, rather than in PT or aPTT assays, these findings indicate that all materials primarily activate coagulation factors through the intrinsic pathway of the coagulation cascade. This is consistent with previously reported data on silicate materials in the literature.[8,9,14]

To further assess the coagulant action of the synthesized materials, the in vitro hemostatic activities of the zeolitic materials were evaluated by thromboelastography (TEG), which provides a global estimation of hemostasis by quantitatively measuring the viscoelastic changes in whole blood during the coagulation process, where the main parameters considered are *R*, α, *K*, and MA. The time until the curve of the clot strength splits, *R*, represents the time for initial detection of clot formation. The α parameter is the angle between the tangent to the rising curve and the horizontal. The *K* parameter is related to the rate of coagulation, while MA is the maximum amplitude of the viscosity curve split, representing the maximum clot strength. The tests showed that all the synthesized calcium-silicate materials were able to promote faster clot formation ($R = 1.8$ min) and higher maximum clot strength (MA = 52.1 mm), compared to the commercial QuikClot material ($R = 2.7$ min, MA = 47.5 mm; $p < 0.05$). **Figure 9** shows the TEG plots for all the calcium-silicates prepared in this study. The thromboelastographic parameter values are shown in **Table 2**.

The values obtained for *R* and MA were superior to, or close to, those reported in the literature for topical hemostatic agents based on zeolites and other inorganic materials (**Table 3**). The initial clot formation time (*R* parameter) was consistent with previous observations for hemostatic agents based on faujasite zeolite,[13,65] LTA zeolite,[24] mesoporous silica spheres,[66] and mesoporous silica nanoparticles.[67] Similarly, the maximum clot strength (MA parameter) values for the calcium-silicates prepared here were within the range reported for other hemostatic agents based on zeolites.[13,24,65]

Phase-contrast microscopy was utilized to assess the interaction between red blood cells and CaZ-4, the calcium-silicate material synthesized in this study that exhibited the highest

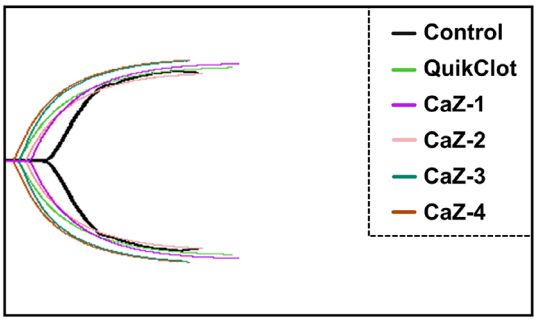

Figure 9. Thromboelastography (TEG 5000, Haemonetics, Niles, IL, USA) curves of human blood after contact with QuikClot and calcium silicate materials CaZ-1, CaZ-2, CaZ-3, and CaZ-4. The control curve corresponds to human blood without exposure to any hemostatic agent.

Table 2. Clotting kinetic parameters (*R*, *K*, α, and MA) for human blood using the hemostatic agents QuikClot and the synthesized calcium-silicate materials. The control corresponds to human blood not exposed to the hemostatic agents.

Material	R [min]	K [min]	Alpha Angle [°]	MA [mm]
Control	7.4 ± 0.8	3.3 ± 0.5	48.5 ± 6.6	46.6 ± 2.4
QuikClot	2.7 ± 0.4	3.6 ± 0.3	54.6 ± 6.8	47.5 ± 0.9
CaZ-1	4.5 ± 0.7	3.2 ± 0.6	55.5 ± 5.9	49.2 ± 1.7
CaZ-2	3.8 ± 0.3	3.6 ± 0.2	54.9 ± 5.7	44.9 ± 3.3
CaZ-3	2.7 ± 0.4	2.6 ± 0.2	60.3 ± 6.1	51.5 ± 2.0
CaZ-4	1.8 ± 0.5	2.8 ± 0.4	56.8 ± 5.7	52.1 ± 1.3

Table 3. Comparison of thromboelastographic parameters reported in the literature for inorganic hemostatic agents.

Material	R [min]	MA [mm]
FAU[13]	3.2 ± 0.7	53.6 ± 2.6
Nano-FAU[13]	2.4 ± 0.6	61.2 ± 2.3
CaO/sodium dodecyl sulfate (SDS) + 1% NaY[65]	7.2 ± 0.9	52.1 ± 1.4
CaO/sodium dodecyl sulfate (SDS) + 5% NaY[65]	6.2 ± 0.3	53.9 ± 1.8
Ba-exchanged LTA zeolite[24]	1.8 ± 0.2	76.9 ± 1.2
Sr-exchanged LTA zeolite[24]	2.1 ± 0.2	73.7 ± 2.6
Pure mesoporous silica spheres (MSS)[66]	3.6 ± 0.4	58.7 ± 1.7
AgCaMSS (MSS doped with silver and calcium)[66]	2.9 ± 0.2	66.0 ± 3.3
Mesoporous silica nanoparticles (MSN)[67]	6.9 ± 0.3	67.3 ± 2.1
CaMSN (MSN doped with calcium)[67]	4.5 ± 0.3	73.5 ± 3.6
CaZ-4 (prepared with chicken eggshell waste in this study)	1.8 ± 0.5	52.1 ± 1.3

© 2025 The Author(s). European Journal of Inorganic Chemistry published by Wiley-VCH GmbH

Research Article
doi.org/10.1002/ejic.202500227

10990682c, 2025, 26, Downloaded from https://chemistry-europe.onlinelibrary.wiley.com/doi/10.1002/ejic.202500227 by University Of Sao Paulo - Brazil, Wiley Online Library on [29/09/2025]. See the Terms and Conditions (https://onlinelibrary.wiley.com/terms-and-conditions) on Wiley Online Library for rules of use; OA articles are governed by the applicable Creative Commons License

coagulant efficiency. Figure SF15A (see Supporting Information) depicts red blood cells in pure whole blood prior to the addition of CaZ-4, displaying their characteristic morphology, including a circular shape, biconcave structure, and a diameter of 6−8 μm.[13] Following exposure to CaZ-4, the red blood cells aggregate, forming a dense clot that appears as a solid mass of blood cells, as illustrated in Figure SF15B, Supporting Information. This observation confirms clot formation, underscores the capacity of calcium-silicate materials to accelerate blood coagulation, and corroborates the findings from thromboelastographic assays.

3. Conclusion

1) Under specific physicochemical conditions, utilizing TBA.OH and TPA.OH as organic templates, chicken eggshell waste can serve as a precursor for synthesizing rhodesite calcium-silicate. 2) When TEA.OH was employed under the same sol-gel conditions, the resulting material consisted of quartz and unidentified crystalline phases. 3) BET-N_2 analysis of the calcium-silicates synthesized with TBA.OH and TPA.OH revealed surface areas of 100.3 and 72.2 $m^2\,g^{-1}$, pore volumes of 0.11 and 0.10 $cm^3\,g^{-1}$, and pore diameters of 57.1 and 67.4 Å, respectively. 4) Rhodesite synthesized using TBA.OH as an organic template exhibited a sixfold increase in surface area compared to the rhodesite synthesized by Rocha et al. in the absence of an organic structure-directing agent. 5) In vitro PT and aPTT assays demonstrated that CaZ-3 and CaZ-4 primarily activate coagulation factors within the contact system, consistent with silicate-based materials. The pronounced reduction in clotting time observed in the recalcification assay suggests that their hemostatic action is driven by the intrinsic coagulation pathway. 6) The thromboelastographic parameters for the material synthesized using TBA.OH were: $R = 1.8$ min (latency time for initial fibrin formation at 2 mm clot amplitude), $K = 2.8$ min (time for clot growth to 20 mm), $\alpha = 56.8°$ (rate of thrombin generation and fibrin formation), and MA = 52.1 mm (maximum clot strength reflecting fibrin elasticity and platelet adhesion). 7) These thromboelastographic values surpassed those of the commercially available zeolite-based hemostatic agent QuikClot ($R = 2.7$ min, $K = 3.6$ min, $\alpha = 54.6°$, and MA = 47.5 mm), highlighting superior hemostatic performance. 8) The results demonstrate the feasibility of synthesizing calcium-silicate materials from chicken eggshell waste, offering a sustainable approach for developing effective and safe hemostatic agents.

4. Experimental Section

Chemicals

The preparation of the calcium-silicates employed the following chemicals: distilled water (H_2O), sodium hydroxide pellets (NaOH), calcium carbonate ($CaCO_3$), Ludox-40, tetraethylammonium hydroxide solution (TEA.OH, 20 wt% in H_2O), tetrapropylammonium hydroxide solution (TPA.OH, 1.0 M in H_2O), and tetrabutylammonium hydroxide solution (TBA.OH, 40 wt% in H_2O). $CaCO_3$ was obtained from empty chicken eggshell waste, collected from the Doçura bakery in São José do Rio Preto (São Paulo state, Brazil). The eggshells were washed with warm tap water to remove unwanted material adhered on the surface, rinsed thoroughly with distilled water, and dried in a hot air oven at 100 °C for 24 h. The eggshells were then finely crushed using a blender and passed through a 60 μm mesh sieve.

Syntheses of the Calcium-Silicates

Four different materials were synthesized in this work, according to the same synthesis procedure, but with differences in terms of the structure-directing agent (SDA). The materials were named CaZ-1 (no SDA), CaZ-2 (TEA.OH as SDA), CaZ-3 (TPA.OH as SDA), and CaZ-4 (TBA.OH as SDA). The reagents used for the syntheses were calcium carbonate ($CaCO_3$) from pristine chicken eggshells, sodium hydroxide (NaOH), Ludox-40 (source of silica), TEA.OH, TPA.OH, TBA.OH, and distilled water (H_2O). In a typical synthesis, 3.9 g of NaOH, 0.42 g of CaCO3, 17.4 g of Ludox-40, and 26.7 g of H_2O were added to a Teflon flask and stirred until obtaining a clear homogeneous solution. Addition was then made of 10.6 g of TEA.OH (for CaZ-2), 14.2 g of TPA.OH (for CaZ-3), or 9.1 g of TBA.OH (for CaZ-4), and the mixture was left under stirring for 1 h. The clear homogeneous gel formed was transferred to a Teflon-lined autoclave and heated under autogenous pressure for 72 h at 200 °C in a hot air oven. The product was washed with deionized water, collected by vacuum filtration, and dried in an oven at 80 °C for around 24 h.

Physicochemical Characterization: X-ray Diffraction (XRD)

X-ray diffractograms of the synthesized materials were acquired using a MiniFlex II diffractometer (Rigaku) equipped with a graphite monochromator and a rotary anode source consisting of a flat plate in Bragg-Brentano geometry. The instrument was operated with Cu Kα radiation (wavelength = 1.5418 Å), at 40 kV and 15 mA. The diffractograms were recorded in the 2θ range 3°–50°, at a scan speed of 2° (2θ) min^{-1}.

Physicochemical Characterization: SEM and TEM

SEM images were obtained using a FESEM JSM-7401 F instrument (JEOL). Due to the nonconductive nature of the calcium-silicates, the samples were coated with a thin layer of gold prior to the analyses. SEM images were recorded using FEI Magellan 400 L and Philips XL-30 FEG instruments, both coupled to energy dispersive X-ray (EDS) analyzers and operated with adjustable electron beam voltages from 5 to 25 kV. Prior to the analysis, a thin coating of gold was deposited on the samples. TEM images were acquired with an FEI Tecnai G2 F20 instrument. HRTEM images and corresponding EDX maps were obtained using an FEI Tecnai G2 F20 instrument equipped with an energy-dispersive X-ray spectrometer (EDX) with a super ultra-thin window (SUTW). The experiments were carried out at the Structural Characterization Laboratory of the Federal University of São Carlos (LCE/DEMa/UFSCar).

Physicochemical Characterization: Solid State NMR-MAS

Magic-angle spinning (MAS) solid-state (SS) NMR spectra of ^{29}Si[68] were obtained at the São Carlos Institute of Physics, University of São Paulo, using a Bruker Avance spectrometer operating with a static field of 9.4 T. The instrument was equipped with a 7 mm double resonance Jackobsen design probe head, with a pneumatic sample rotation system, providing frequency stability greater than 2 Hz. Single-pulse excitation experiments under MAS (^{29}Si SPEMAS) were

© 2025 The Author(s). European Journal of Inorganic Chemistry published by Wiley-VCH GmbH

Research Article
doi.org/10.1002/ejic.202500227

performed at 6 kHz MAS frequency, using a recycle delay of 20 s to achieve more quantitative ^{29}Si spectra. Experiments with ^{1}H-^{29}Si cross-polarization (^{1}H-^{29}Si CPMAS) were performed with a power ramp (80%–100%) in the ^{1}H radiofrequency channel, MAS frequency of 6 kHz, and 5 s recycle delay. In both CPMAS and SPEMAS experiments, ^{1}H decoupling was achieved using a SPINAL-64 decoupling pulse sequence, with a field of 60 kHz, during an acquisition time of 15 ms. Zirconia rotors were used in all the experiments, with the absence of background signals confirmed by measuring empty rotors. The ^{29}Si chemical shifts were calibrated using kaolinite as an external reference.

Physicochemical Characterization: ICP-OES

Inductively coupled plasma optical emission spectroscopy (ICP-OES) elemental analysis was performed using a Spectro Arcos spectrometer. Sample digestion was carried out with concentrated hydrofluoric acid, followed by heating on a digester block to ensure complete dissolution of the material.

Physicochemical Characterization: Phase Contrast Microscopy

Phase contrast images were obtained using a BX60 microscope (Olympus, New York, USA). For these analyses, 170 μL of whole blood, collected in tubes containing sodium citrate (4% v/v), was mixed with 10 μL of an aqueous 0.2 M $CaCl_2$ solution to counteract the anticoagulant effect of calcium chelation effect induced by sodium citrate. Subsequently, 0.25 mg of each calcium-silicate material was introduced into the blood, and an aliquot of this mixture was deposited onto glass microscope slides. The slides were then immediately placed under the microscope for structural assessment.

Physicochemical Characterization: FTIR

Fourier-transform infrared spectroscopy (FTIR) spectra were acquired using a Shimadzu IRTracer-100 spectrometer, in the range 400–4000 cm^{-1}, with resolution of 4 cm^{-1}, step size of 1 cm^{-1}, and averaging of 64 scans. The samples were prepared as KBr pellets containing about 10% by weight of the test material.

Physicochemical Characterization: Textural Characterization

Textural characterization of the synthesized calcium-silicates was performed using a Micromeritics ASAP 2020 Plus automatic adsorption apparatus (Accelerated Surface Area and Porosimetry System). Prior to determination of the adsorption isotherm, the samples (≈0.1 g) were outgassed for 12–16 h at 150 °C, until the residual pressure was lower than 5.0 μmHg. Since the samples presented microporosity, a second stage of outgassing with heating was applied after transfer to the instrument port for analysis, to ensure that the micropores were free from moisture or contamination with other vapors. The specific surface area (*S*) values were calculated according to the Brunauer–Emmet–Teller (BET) model.[69] Close to partial pressure $P/P0 = 1$, N_2 condenses in the entire available pore volume (at the end point), so the isotherm provides an indication of the total pore volume. To determine the mesopore scale pore size distribution, the Barret–Joyner–Halenda (BJH) mathematical model was applied, based on the Kelvin equation.[70] For the micropore scale, the average diameter was determined using the Horvath–Kawazoe (H–K) method, which was developed to determine the pore size distribution of graphitic cracks in microporous carbons, using N_2 adsorption measurements at 77 K.[71]

Physicochemical Characterization: Thermogravimetry (TGA/DTG)

Thermogravimetric analyses were performed using a TGA-51 thermobalance (Shimadzu, Japan), under a dynamic air atmosphere (50 mL min^{-1}), with the sample (12–17 mg) placed in a platinum pan and heated at a rate (β) of 10 °C min^{-1}.

Physicochemical Characterization: DSC

Differential scanning calorimetry (DSC) analyses employed a DSC Q20 analyzer (TA Instruments), with the sample placed in an aluminum pan and heated from 25 to 400 °C, at 5 °C min^{-1}, under a flow of nitrogen.

Physicochemical Characterization: Zeta Potential (ζ)

Zeta potential data were obtained using a Nano ZS instrument (Malvern Instruments, Herrenberg, Germany). The zeta potential values were inferred from the electrophoretic mobility measurements with application of the Smoluchowski equation.[9,64,72] ≈2 mg portions of the prepared calcium-silicates were suspended in 2 mL of 2.5 mM calcium nitrate solution (1 wt%) at pH ranging from 1 to 12 (adjusted with 0.25 M solutions of NaOH and HNO_3).

Thromboelastographic Assays

Thromboelastography assays were conducted using a TEG 5000 system (Haemonetics, Niles, IL, USA) with volunteers who were physically healthy and had no history of blood disorders. This analysis was performed to obtain in vitro clotting parameters for whole human blood exposed to the synthesized calcium-silicate hemostatic materials. All participants provided informed consent prior to blood donation. The study was approved by the Research Ethics Committee of FAMERP (São José do Rio Preto Medical School) under protocol number CAAE 48358215.9.0000.5415. For each assay, a 20 μL aliquot of an aqueous 0.2 M $CaCl_2$ solution was added into the TEG sample cup. Separately, 340 μL of whole blood was mixed with 0.5 mg of each calcium-silicate material. The mixture was directly introduced into the TEG sample cup containing the 0.2 M CaCl2 solution. The test was then conducted under standard conditions, with coagulation parameters recorded alongside the corresponding TEG curves.

In Vitro Evaluation of Coagulant Activity

CaZ-3, CaZ-4, and Quickclot were dissolved in Tyrode buffer (137 mM NaCl, 2.7 mM KCl, 3.0 mM NaH2PO4, 10 mM HEPES, 5.6 mM dextrose, 1 mM MgCl2, 2 mM CaCl2, pH 7.4) at the concentration of 1 mg mL^{-1}. Evaluation of coagulant activity was based on the degree of shortening or prolongation of clotting times of prothrombin time (PT, WAMA, Brazil), activated partial thromboplastin time (aPTT, WAMA, Brazil), or recalcification time of pooled citrated human plasma.[73] For PT assays, aliquots of 50 μL of the plasma sample were incubated with 50 μL of material suspension or vehicle control (Tyrode buffer, negative control), incubated at 37 °C for 2 min; following incubation 100 μL of PT reagent was added, and the clotting time recorded. For the recalcification time, aliquots of 50 μL of the plasma sample were incubated with 50 μL of material suspension or vehicle control (Tyrode buffer, negative control), incubated at 37 °C for 2 min; following incubation, then 50 μL of 25 mM CaCl2 was added, and the clotting time recorded. For aPTT assays, aliquots of 50 μL of the plasma sample

© 2025 The Author(s). European Journal of Inorganic Chemistry published by Wiley-VCH GmbH

10990682c, 2025, 26, Downloaded from https://chemistry-europe.onlinelibrary.wiley.com/doi/10.1002/ejic.202500227 by University Of Sao Paulo - Brazil, Wiley Online Library on [29/09/2025]. See the Terms and Conditions (https://onlinelibrary.wiley.com/terms-and-conditions) on Wiley Online Library for rules of use; OA articles are governed by the applicable Creative Commons License

were incubated with 50 μL of material suspension or vehicle control (Tyrode buffer, negative control) and 50 μL of aPTT reagent; following incubation at 37 °C for 3 min, 50 μL of 25 mM CaCl2 was added and the clotting time recorded. Clotting times were determined in a coagulometer Coagmaster 2.0 (WAMA, Brazil), and recorded up to a maximum of 200 s.

Statistical Analysis

Descriptive statistical analysis of the synthesized materials was conducted using mean values and standard deviations. For inferential statistical analysis, one-way analysis of variance was employed to compare the mean values of each group at a significance level of $p \leq 0.05$. When statistically significant differences were identified, multiple comparisons were carried out using the Tukey–Kramer post hoc test.

Acknowledgements

The authors acknowledge the Coordination for the Improvement of Higher Education Personnel (CAPES) for financial support through fellowships awarded to G.P. Guarnieri (grant #88887.661419/2022-00), O.A.N. Santisteban (grant #88882.434369/2019–01), E.P. Cancella (grant #88887.513909/2020-00), and L.P. Mercuri (grant #88881.120798/2016-01). Additionally, L.P. Mercuri received research funding from the National Council for Scientific and Technological Development (CNPq, Grant #430922/2016-7). The authors also express gratitude to CNPq for the financial support provided to E.R. Azevedo (grant #308760/2022-0), M.L. Santoro (grant #309980/2021-6), and J.G. Nery (grant #406761/2013-2). Support from the São Paulo Research Foundation (FAPESP) is acknowledged for the multi-user project "ASAP2020 Plus" (grant #2018/19251-7, I.C. Cosentino) and for research funding awarded to J.G. Nery (grants #2019/01858-5 and #2022/16214-9). We thank Adrielly Viveiros Torres and Natacha Ferreira de Oliveira (School of Medicine, University of São Paulo – FMUSP, Brazil) for their assistance with the PT and aPTT coagulation assays.

The Article Processing Charge for the publication of this research was funded by the Coordenação de Aperfeiçoamento de Pessoal de Nível Superior - Brasil (CAPES) (ROR identifier: 00x0ma614).

Conflict of Interest

The authors declare no conflict of interest.

Data Availability Statement

The data that support the findings of this study are available from the corresponding author upon reasonable request.

Keywords: biomass · calcium · chicken eggshell waste · mesoporous materials · zeolite analogues

[1] B. J. Eastridge, R. L. Mabry, P. Seguin, J. Cantrell, T. Tops, P. Uribe, O. Mallett, T. Zubko, L. Oetjen-Gerdes, T. E. Rasmussen, F. K. Butler, R. S. Kotwal, J. B. Holcomb, C. Wade, H. Champion, M. Lawnick, L. Moores, L. H. Blackbourne, *J. Trauma Acute Care Surg.* **2012**, *73*, S431.
[2] B. Mitra, B. J. Gabbe, K. M. Kaukonen, A. Olaussen, D. J. Cooper, P. A. Cameron, *Shock* **2014**, *42*, 307.
[3] D. M. Monroe, M. Hoffman, *Arterioscler. Thromb. Vasc. Biol.* **2006**, *26*, 41.
[4] R. L. Gruen, K. Brohi, M. Schreiber, Z. J. Balogh, V. Pitt, M. Narayan, R. V. Maier, *The Lancet* **2012**, *380*, 1099.
[5] D. S. Kauvar, R. Lefering, C. E. Wade, *J. Trauma:Inj., Infect., Crit. Care* **2006**, *60*, S3.
[6] A. E. Pusateri, J. B. Holcomb, B. S. Kheirabadi, H. B. Alam, C. E. Wade, K. L. Ryan, *The J. Trauma:Inj., Infect., Crit. Care* **2006**, *60*, 674.
[7] P. Rhee, C. Brown, M. Martin, A. Salim, D. Plurad, D. Green, L. Chambers, D. Demetriades, G. Velmahos, H. Alam, *J. Trauma:Inj., Infect., Crit. Care* **2008**, *64*, 1093.
[8] S. Pourshahrestani, E. Zeimaran, I. Djordjevic, N. A. Kadri, M. R. Towler, *Mater. Sci. Eng.: C* **2016**, *58*, 1255.
[9] T. A. Ostomel, Q. Shi, P. K. Stoimenov, G. D. Stucky, *Langmuir* **2007**, *23*, 11233.
[10] X. Shang, H. Chen, V. Castagnola, K. Liu, L. Boselli, V. Petseva, L. Yu, L. Xiao, M. He, F. Wang, K. A. Dawson, J. Fan, *Nat. Catal.* **2021**, *4*, 607.
[11] C. Shi, M. He, H. Chen, X. Wei, L. Xiao, X. Shang, Y. Shi, Q. Wang, L. Yu, J. Fan, *Adv. Sci.* **2025**, *12*, 2417099.
[12] Y. Guo, M. Wang, Q. Liu, G. Liu, S. Wang, J. Li, *Theranostics* **2023**, *13*, 161.
[13] J. B. Laurenti, G. Zazeri, A. P. R. Povinelli, M. F. de Godoy, D. M. Braile, T. R. F. da Rocha, É. A. D'Amico, J. G. Nery, *Microporous Mesoporous Mater.* **2017**, *239*, 263.
[14] Y. Zheng, J. Wu, Y. Zhu, C. Wu, *Chem. Sci.* **2023**, *14*, 29.
[15] S. E. Baker, A. M. Sawvel, N. Zheng, G. D. Stucky, *Chem. Mater.* **2007**, *19*, 4390.
[16] H. Shao, X. Wu, J. Deng, Y. Yang, W. Chen, K. Li, X. Xie, H. She, W. Jian, H. Li, J. Ma, *J. Mater. Sci.* **2024**, *59*, 7169.
[17] G.de P. Guarnieri, J. G. Nery, *J. Mater. Sci. Technol. Res.* **2024**, *11*, 90.
[18] A. Merchant, S. Batzner, S. S. Schoenholz, M. Aykol, G. Cheon, E. D. Cubuk, *Nature* **2023**, *624*, 80.
[19] A. Pihlajamäki, M. F. Matus, S. Malola, H. Häkkinen, *Adv. Mater.* **2024**, *36*, 2407046.
[20] F. Arnaud, T. Tomori, W. Carr, A. McKeague, K. Teranishi, K. Prusaczyk, R. McCarron, *Ann. Biomed. Eng.* **2008**, *36*, 1708.
[21] H. Khoshmohabat, B. Dalfardi, A. Dehghanian, H. R. Rasouli, S. M. J. Mortazavi, S. Paydar, *J. Surg. Res.* **2016**, *200*, 732.
[22] K. R. Ward, M. H. Tiba, W. H. Holbert, C. R. Blocher, G. T. Draucker, E. K. Proffitt, G. L. Bowlin, R. R. Ivatury, R. F. Diegelmann, *J. Trauma:Inj., Infect., Crit. Care* **2007**, *63*, 276.
[23] M. Alavi, A. Totonchi, M. A. Okhovat, M. Motazedian, P. Rezaei, M. Atefi, *Blood Coagulation Fibrinolysis* **2014**, *25*, 856.
[24] T. A. Ostomel, P. K. Stoimenov, P. A. Holden, H. B. Alam, G. D. Stucky, *J. Thromb. Thrombolysis* **2006**, *22*, 55.
[25] H. M. H. Spronk, J. W. P. Govers-Riemslag, H. ten Cate, *BioEssays* **2003**, *25*, 1220.
[26] C. Baerlocher, L. McCusker, *Database of Zeolite Structures, Structure*, http://www.iza-structure.org/database/.
[27] S. Fernandez, M. L. Ostraat, K. Zhang, *AIChE J.* **2020**, *66*, e16943.
[28] H. Serati-Nouri, A. Jafari, L. Roshangar, M. Dadashpour, Y. Pilehvar-Soltanahmadi, N. Zarghami, *Mater. Sci. Eng.: C* **2020**, *116*, 111225.
[29] L. Bacakova, M. Vandrovcova, I. Kopova, I. Jirka, *Biomater. Sci.* **2018**, *6*, 974.
[30] I. Kiseleva, A. Navrotsky, I. Belitsky, B. Fursenko, *Am. Mineral.* **2001**, *86*, 448.
[31] U. Wirsching, *Clays Clay Miner.* **1981**, *29*, 171.
[32] S. Khodabandeh, M. E. Davis, *Microporous Mater.* **1997**, *9*, 161.
[33] S. J. Chipera, J. A. Apps, *Rev. Mineral. Geochem.* **2001**, *45*, 117.
[34] T. A. E. Ahmed, L. Wu, M. Younes, M. Hincke, *Front. Bioeng. Biotechnol.* **2021**, *9*, 675364.
[35] S. A. Singh, C. Vellapandian, D. D. Shah, T. J. Jayeoye, M. R. Chorawala, S. Singh, B. G. Prajapati, *Waste Biomass Valorization* **2024**, *15*, 1917.
[36] P. R. Pandit, M. H. Fulekar, *J. Environ. Manage.* **2017**, *198*, 319.
[37] G. Sharma, M. Kaur, S. Punj, K. Singh, *Biofuels, Bioprod. Biorefin.* **2020**, *14*, 673.
[38] I. Tobío-Pérez, Y. D. Domínguez, L. R. Machín, S. Pohl, M. Lapuerta, R. Piloto-Rodríguez, *Int. J. Energy Res.* **2022**, *46*, 3782.
[39] L. Habte, N. Shiferaw, D. Mulatu, T. Thenepalli, R. Chilakala, J. Ahn, *Sustainability* **2019**, *11*, 3196.

© 2025 The Author(s). European Journal of Inorganic Chemistry published by Wiley-VCH GmbH

10990682c, 2025, 26, Downloaded from https://chemistry-europe.onlinelibrary.wiley.com/doi/10.1002/ejic.202500227 by University Of Sao Paulo - Brazil, Wiley Online Library on [29/09/2025]. See the Terms and Conditions (https://onlinelibrary.wiley.com/terms-and-conditions) on Wiley Online Library for rules of use; OA articles are governed by the applicable Creative Commons License

[40] M. E. Torres Gouveia, C. Milhans, M. Gezek, G. Camci-Unal, *Adv. Nanobiomed. Res.* **2025**, *5*, 2400120.
[41] J. A. Gard, H. F. W. Taylor, R. A. Chalmers, *Mineral. Mag. J. Mineral. Soc.* **1957**, *31*, 611.
[42] K.-F. Hesse, F. Liebau, S. Merlino, *Zeitschrift für Kristallographie* **1992**, *199*, 25.
[43] J. Rocha, P. Ferreira, Z. Lin, P. Brandão, A. Ferreira, J. D. Pedrosa de Jesus, *J. Phys. Chem. B* **1998**, *102*, 4739.
[44] R. F. Munhá, D. Ananias, F. A. A. Paz, J. Rocha, *Z. Kristallogr. Cryst. Mater.* **2015**, *230*, 353.
[45] J. Rocha, M. W. Anderson, *Eur. J. Inorg. Chem.* **2000**, *2000*, 801.
[46] R. Bai, Q. Sun, N. Wang, Y. Zou, G. Guo, S. Iborra, A. Corma, J. Yu, *Chem. Mater.* **2016**, *28*, 6455.
[47] G. Ferraris, *Rev. Mineral. Geochem.* **2005**, *57*, 69.
[48] G. Ferraris, E. Belluso, A. Gula, S. V. Soboleva, A. P. Khomyakov, *The Can. Mineral.* **2003**, *41*, 1183.
[49] G. Geng, Z. Shi, A. Leemann, C. Borca, T. Huthwelker, K. Glazyrin, I. V. Pekov, S. Churakov, B. Lothenbach, R. Dähn, E. Wieland, *Cem. Concr. Res.* **2020**, *129*, 105958.
[50] E. M. Flanigen, H. Khatami, H. A. Szymanski, in *Molecular Sieve Zeolites-I* (Eds: E. M. Flanigen, L. B. Sand), American Chemical Society, Washinton, DC **1974**, pp. 201–229.
[51] M. Król, W. Mozgawa, J. Morawska, W. Pichór, *Microporous Mesoporous Mater.* **2014**, *196*, 216.
[52] R. Choudhary, S. Koppala, S. Swamiappan, *J. Asian Ceram. Soc.* **2015**, *3*, 173.
[53] R. Choudhary, S. K. Venkatraman, I. Bulygina, A. Chatterjee, J. Abraham, F. Senatov, S. Kaloshkin, A. Ilyasov, M. Abakumov, M. Knyazeva, D. Kukui, F. Walther, S. Swamiappan, *J. Asian Ceram. Soc.* **2020**, *8*, 1051.
[54] A. Sobhani, E. Salimi, *Sci. Rep.* **2023**, *13*, 16330.
[55] F. A. Andersen, L. Brecevic, *Acta Chem. Scand.* **1991**, *45*, 1018.
[56] S. Elderderi, C. Leman-Loubière, L. Wils, S. Henry, D. Bertrand, H. J. Byrne, I. Chourpa, C. Enguehard-Gueiffier, E. Munnier, A. A. Elbashir, L. Boudesocque-Delaye, F. Bonnier, *J. Mol. Liq.* **2020**, *311*, 113361.
[57] F. Cheng, Q. Cao, Y. Guan, H. Cheng, X. Wang, J. D. Miller, *Int. J. Miner. Process.* **2013**, *122*, 36.
[58] S. Lima, A. S. Dias, Z. Lin, P. Brandão, P. Ferreira, M. Pillinger, J. Rocha, V. Calvino-Casilda, A. A. Valente, *Appl. Catal. A Gen.* **2008**, *339*, 21.
[59] C. T. Kresge, M. E. Leonowicz, W. J. Roth, J. C. Vartuli, J. S. Beck, *Nature* **1992**, *359*, 710.
[60] A. Corma, *Chem. Rev.* **1997**, *97*, 2373.
[61] J. H. Griffin, *Proc. Natl. Acad. Sci.* **1978**, *75*, 1998.
[62] G. D. Stucky, T. A. Ostomel, Q. Shi, P. K. Stoimenov, P. A. Holden, US7858123B2, **2006**.
[63] M. Hoffman, *J. Thromb. Thrombolysis* **2003**, *16*, 17.
[64] T. Kuzniatsova, Y. Kim, K. Shqau, P. K. Dutta, H. Verweij, *Microporous Mesoporous Mater.* **2007**, *103*, 102.
[65] J. V. Edwards, N. T. Prevost, M. S. Cintron, *J. Funct. Biomater.* **2023**, *14*, 255.
[66] C. Dai, Y. Yuan, C. Liu, J. Wei, H. Hong, X. Li, X. Pan, *Biomaterials* **2009**, *30*, 5364.
[67] S. Ding, X. Wei, K. Yang, S. Lin, F. Tian, F. Li, *Silicon* **2021**, *13*, 4033.
[68] G. Engelhardt, H. Koller, in *Solid-State NMR II: Inorganic Matter*, Springer Berlin Heidelberg, Berlin, Heidelberg **1994**, pp. 1–29.
[69] S. Brunauer, P. H. Emmett, E. Teller, *J. Am. Chem. Soc.* **1938**, *60*, 309.
[70] E. P. Barrett, L. G. Joyner, P. P. Halenda, *J. Am. Chem. Soc.* **1951**, *73*, 373.
[71] G. HORVÁTH, K. KAWAZOE, *J. Chem. Eng. Japan* **1983**, *16*, 470.
[72] M. Alkan, Ö. Demirbaş, M. Doğan, *J. Colloid Interface Sci.* **2005**, *281*, 240.
[73] M. L. Santoro, M. C. C. Sousa-e-Silva, L. R. C. Gonçalves, S. M. Almeida-Santos, D. F. Cardoso, I. L. Laporta-Ferreira, M. Saiki, C. A. Peres, I. S. Sano-Martins, *Comp. Biochem. Physiol., C: Pharmacol., Toxicol. Endocrinol.* **1999**, *122*, 61.
[74] S. A. Smith, R. J. Travers, J. H. Morrissey, *Crit. Rev. Biochem. Mol. Biol.* **2015**, *50*, 326.
[75] M. Hoffman, D. Monroe, *Thromb. Haemost.* **2001**, *85*, 958.

Manuscript received: April 30, 2025
Revised manuscript received: July 31, 2025
Version of record online: September 9, 2025

10990682c, 2025, 26, Downloaded from https://chemistry-europe.onlinelibrary.wiley.com/doi/10.1002/ejic.202500227 by University Of Sao Paulo - Brazil, Wiley Online Library on [29/09/2025]. See the Terms and Conditions (https://onlinelibrary.wiley.com/terms-and-conditions) on Wiley Online Library for rules of use; OA articles are governed by the applicable Creative Commons License

© 2025 The Author(s). European Journal of Inorganic Chemistry published by Wiley-VCH GmbH